Strongly coupled van der Waals heterostructures for high-performance infrared phototransistor 🄵

Ningning Li, Yao Wen, Ruiqing Cheng, Lei Yin, Feng Wang, Jie Li, Tofik Ahmed Shifa, Liping Feng, Zhenxing Wang, and Jun He

COLLECTIONS

🄵 This paper was selected as Featured

View Online   Export Citation   CrossMark

ARTICLES YOU MAY BE INTERESTED IN

Strongly coupled van der Waals heterostructures for high-performance infrared phototransistor (F)

Ningning Li,[1,2,3,a)] Yao Wen,[2,4,a)] Ruiqing Cheng,[1,2] Lei Yin,[1,2] Feng Wang,[1,2] Jie Li,[1,2] Tofik Ahmed Shifa,[1,2]
Liping Feng,[5,b)] Zhenxing Wang,[1,b)] and Jun He[1,b)]

AFFILIATIONS

[1]CAS Center for Excellence in Nanoscience, CAS Key Laboratory of Nanosystem and Hierarchical Fabrication, National Center for Nanoscience and Technology, Beijing 100190, People's Republic of China
[2]University of Chinese Academy of Sciences, Beijing 100049, People's Republic of China
[3]Sino-Danish Center for Education and Research, Beijing 100190, People's Republic of China
[4]CAS Center for Excellence in Nanoscience, CAS Key Laboratory for Standardization and Measurement for Nanotechnology, National Center for Nanoscience and Technology, Beijing 100190, People's Republic of China
[5]State Key Lab Solidification Processing, College of Materials Science and Engineering, Northwestern Polytechnical University, Xi'an, Shaanxi 710072, People's Republic of China

[a)]**Contributions:** N. Li and Y. Wen contributed equally to this work.
[b)]**Electronic addresses:** lpfeng@nwpu.edu.cn; wangzx@nanoctr.cn; and hej@nanoctr.cn.

ABSTRACT

The interfacial coupling in van der Waals (vdWs) heterostructures can effectively modulate the device performance. In this study, we demonstrate a high performance infrared detector fabricated by direct epitaxial growth of Te nanowires onto a MoS_2 monolayer. Such directly grown Te/MoS_2 heterostructures show much stronger interfacial coupling than artificially transferred Te/MoS_2 hybrids, as evidenced from their Raman and photoluminescence spectra. The strong vdWs interfacial coupling leads to a high performance infrared detector with both ultrahigh photoresponsivity ($>10^3$ A/W) and rapid response time ($\tau_{rising} = 15$ ms) at the telecommunication wavelength of 1550 nm. The anti-bipolar and rectification behaviors observed in the strongly coupled grown $Te-MoS_2$ heterojunction further confirm the effective interfacial coupling. In contrast, the weakly coupled transferred $Te-MoS_2$ heterojunction that is obtained by artificial transfer exhibits negligible anti-bipolar behavior and slight rectification behavior. These findings indicate that the coupled vdWs hybrid structures have great potential for achieving high performance photodetectors.

Published under license by AIP Publishing. https://doi.org/10.1063/1.5083685

Photodiodes based on 2D van der Waals (vdWs) heterostructures, such as BP/MoS_2,[1] BP/WSe_2,[2] and $MoTe_2/MoS_2$,[3] have been demonstrated in infrared photodetection. Such vdWs heterostructures show a high-quality interface, benefiting from atomically smooth surfaces without dangling bonds. This feature provides a versatile platform to explore their optoelectronic properties. However, they always exhibit very low responsivity because of the absence of internal gain.[4–6] To significantly improve the gain, hybrid structures based on colloidal quantum dots (CQDs) and 2D materials have been developed. The pioneer work in this framework includes the combination of PbS QDs with graphene,[7,8] MoS_2,[9] and WSe_2.[10] Although high gain was obtained, the poor-quality interfaces, suffering from the weakly interfacial coupling and trap states in the interfaces, lead to very slow response speed.[11–13] In addition, the loosely contacted interface can broaden the vdWs gap in the interface and further increase the tunnel barrier of carriers from CQDs to 2D materials.[14] So far, the realization of high responsivity along with rapid response speed has remained an unresolved issue for the above strategies. Fortunately, the strong vdWs coupling can effectively contribute to the interlayer charge transfer and improve the device performance.[12] Therefore, integrating a high-quality and strong-coupled heterointerface into a vdWs hybrid structure is a crucial subject to produce efficient infrared detectors with both fast response speed and high responsivity.

Here, we demonstrate a high performance infrared phototransistor in a coupled hybrid vdWs structure with high-quality interface. Te nanowires, a typical narrow bandgap semiconductor ($E_g = 0.35$ eV),[15,16] were directly grown on the surface of MoS_2 nanosheets via vdWs epitaxy. The effective interfacial coupling between the Te layer and

the MoS_2 layer, combined with the strong infrared absorption in Te nanowires, results in ultrahigh photoresponsivity ($>10^3$ A/W) as well as fast response time ($\tau_{rising} = 15$ ms) at the telecommunication wavelength of 1550 nm. These results indicate that our coupled vdWs hybrid structures have significant potential for the next generation high-performance infrared detectors.

Figure 1(a) presents the schematic illustration of the epitaxial growth of Te nanowires-MoS_2 heterostructures. Monolayer MoS_2 was first prepared on silicon substrates with 300 nm thick SiO_2 by chemical vapor deposition (CVD). Then, the pre-grown MoS_2 was used for the subsequent epitaxial growth of Te nanowires *via* physical vapor deposition (PVD). (More details are given in the supplementary material.) Te has a typical helical chain-like crystal structure. The atoms in the adjacent chains are combined by weak vdWs forces,[17] which enable the high-quality vdWs heterointerface between Te and MoS_2. The scanning electron microscopy (SEM) image of the grown Te-MoS_2 heterostructure is shown in Fig. 1(b). Interestingly, Te nanowires have three specific growth orientations on MoS_2 with an angular interval of 60°. Figure 1(c) exhibits the histogram statistics of the oriented angle
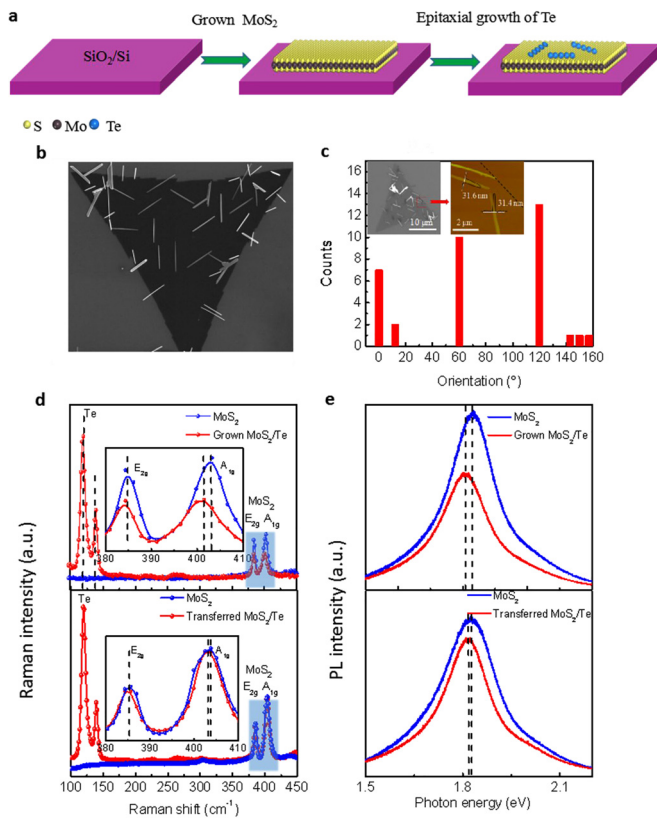

FIG. 1. (a) Schematic illustration of two-step epitaxial growth of Te nanowires-MoS_2 heterostructures. (b) SEM image of epitaxial Te nanowires-MoS_2 heterostructures. The scale bar is 5 μm. (c) The histogram statistics of the orientation distribution of Te nanowires obtained from the left inset. Left inset: the optical microscope (OM) image of Te nanowires-MoS_2 heterostructure. Right inset: the corresponding AFM image and height profiles. (d) Raman and (e) PL spectra of individual MoS_2, grown Te nanowires-MoS_2 and transferred Te nanowires-MoS_2 heterostructures. The inset in figure (d) shows the details of the marked blue region.

distribution of Te nanowires, in which 86% of the nanowires follow three specific directions. Compared to the previous hybrid QDs system with a random distribution, the oriented Te nanowires have much stronger interaction with MoS_2.[18] The chemical states and the composition of nanowires were confirmed by X-ray photoelectron spectroscopy (XPS) analysis. As shown in Fig. S1 in the supplementary material, the peaks at 584.1 and 573.7 eV correspond to Te $3d_{3/2}$ and $3d_{5/2}$, while the other two peaks are attributed to tellurium oxide produced by surface oxidation.[19,20] The thickness of Te nanowires and MoS_2 nanosheets was characterized by atomic force microscopy (AFM). The right inset of Fig. 1(c) shows the AFM image and the height profile of two typical Te nanowires, in which the thickness is identified to be 31.4 and 31.6 nm. The AFM image of monolayer MoS_2 prepared by CVD is shown in Fig. S2 in the supplementary material. To characterize the interfacial coupling between the Te layer and the MoS_2 layer, Raman and photoluminescence (PL) spectroscopy were conducted. Two types of Te-MoS_2 interfaces were constructed: (i) a Te-MoS_2 heterostructure prepared by direct epitaxial growth and (ii) a Te-MoS_2 heterostructure fabricated by artificially stacking Te nanowires onto MoS_2. Raman spectroscopy is a sensitive tool to accurately characterize the interlayer coupling in vdWs heterostructures.[21] Figure 1(d) shows the Raman spectrum of individual MoS_2 and the two types of Te-MoS_2 vdWs heterostructures. In the as-grown Te-MoS_2 vdWs heterostructures, the A_1 (~119.6 cm^{-1}) and E_1 (~139.1 cm^{-1}) modes of Te[22,23] as well as the out-of-plane A_{1g} (~400.9 cm^{-1}) and in-plane E_{2g} (~384.2 cm^{-1}) modes of monolayer MoS_2 are observed. Compared with the individual monolayer MoS_2 ($A_{1g} \sim 403.4$ cm^{-1} and $E_{2g} \sim 384.9$ cm^{-1}), the A_{1g} and E_{2g} peaks in overlapped MoS_2 were red-shifted, indicating the electron transfer from the Te layer to the MoS_2 layer at the interface.[4,24,25] A_{1g} shows a distinct red shift (~2.5 cm^{-1}), but only a slight red shift is observed in the E_{2g} peak; this is because electrons are coupled more tightly with A_{1g} photons than E_{2g} photons.[25] And, the decrease in A_{1g} peak intensity can be attributed to the stacking of Te nanowires on MoS_2, which can restrain its out-of-plane vibration.[24] But, for artificially transferred Te-MoS_2 heterostructures, some polymer residues were left and ambient gases were trapped at the interface during the transfer process, forming a weak interface, and thus the changes in the Raman frequencies are negligible. The corresponding PL spectrum is depicted in Fig. 1(e). The exciton peak A is prominently redshifted and PL intensity is reduced in the grown heterostructure compared with individual MoS_2, which indicate the efficient charge transfer at the interface of Te and MoS_2.[25,26] The excess electrons transferred from Te can effectively combine with excitons in MoS_2 and form the negative trions, thus lowering the charge recombination and peak intensity of exciton A. But only a slight change is observed in the transferred Te-MoS_2 heterostructure due to weak interfacial coupling.

Figure 2(a) shows the schematic diagram of the hybrid phototransistor, in which Te nanowires are designed as the infrared absorber layer and MoS_2 is used as the conducting channel. The electrodes were fabricated by standard electron-beam lithography (EBL) and thermal evaporation of Cr/Au (10/60 nm). The gate voltage was applied to the heavily n-doped silicon substrate. The length and the width of the channel in our device are 3.8 μm and 21.2 μm, respectively. The corresponding power density-dependent transfer curves (I_{ds}-V_{gs}) at the 1550 nm laser are given in Fig. 2(b). Under laser illumination, there is a noticeable increase in the drain current even with an ultralow power
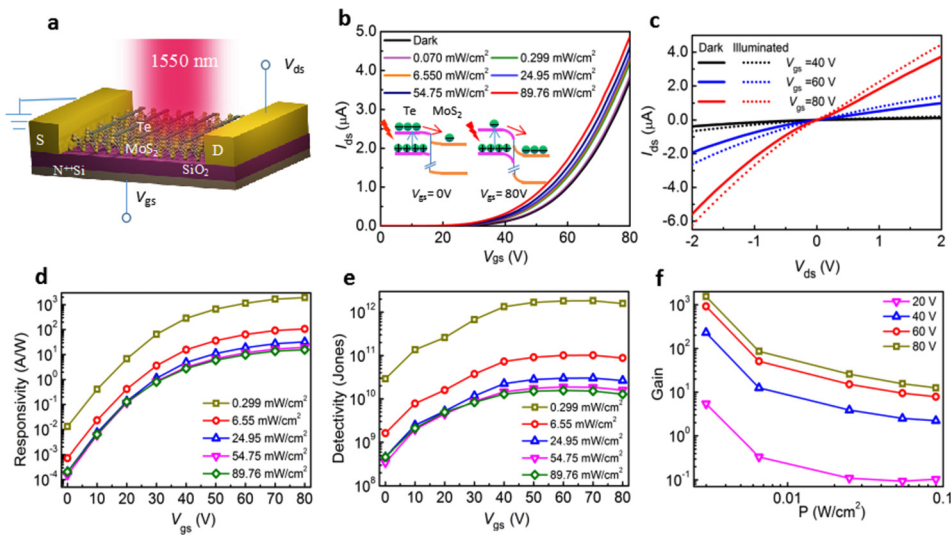
FIG. 2. (a) Schematic of our Te nanowires-MoS$_2$ hybrid phototransistor. Te nanowires and the MoS$_2$ nanosheet act as the infrared absorber layer and the transport channel, respectively. (b) Transfer characteristic (I_{ds}–V_{gs}) curves under illumination of a 1550 nm laser with different power densities ($V_{ds} = 2$ V), the inset shows the energy band diagrams at the junction formed by Te and MoS$_2$ under $V_{gs} = 0$ V and 80 V. (c) Output characteristic (I_{ds}–V_{ds}) curves under dark and illumination states. (d) Responsivity and (e) detectivity of the heterostructures are plotted as a function of V_{gs}. (f) Plots of photoconductive gain (G) versus power density at different V_{gs}.

density of 0.07 mW/cm^2 at 80 K. CVD-grown MoS$_2$ indeed has much various structural defects due to growth process imperfections. However, the photoresponse of the individual MoS$_2$ device under a 1550 nm laser was also measured in Fig. S3(a) in the supplementary material, which is negligible compared with the Te/MoS$_2$ hybrid device due to the intrinsic band gap limitation, and no obvious damage to MoS$_2$ is observed after growth of Te nanowires [Figs. S3(b) and S3(c) in the supplementary material]. Moreover, an individual Te nanowire shows obvious photoresponse at 1550 nm (Fig. S4 in the supplementary material). Thus, the photo-generated carriers mainly originate from Te nanowires in our hybrid device. Driven by the vertical built-in field between Te and MoS$_2$, photo-generated electrons in Te nanowires are transferred to the MoS$_2$ channel, while the holes are confined in the Te nanowires due to the potential barrier at the interface.[27] This directly leads to the increase in the MoS$_2$ channel current. The obvious photoresponse is also reflected in the output curves, as displayed in Fig. 2(c). The relationship of photocurrent ($I_{ph} = I_{light} - I_{dark}$) and power densities at different gate voltages is plotted in Fig. S5 in the supplementary material, in which I_{ph} increases monotonically with the power densities.

To accurately evaluate the device performance, responsivity (R), which is defined as

$$R = \frac{I_{ph}}{PS},$$ (1)

where P is the power density and S is the effective illumination area, was extracted to further quantify the photoresponse performance. As displayed in Fig. 2(d), responsivity increases with the gate voltage, and the maximum responsivity of 10^3 A/W is obtained under $V_{gs} = 80$ V and $P = 0.299$ mW/cm^2. Owing to the electric field screening effect from the underneath MoS$_2$, the applied V_{gs} mainly regulates the Fermi level of MoS$_2$ and leaves the upper Te unaffected.[28,29] Since MoS$_2$ is already in the depletion region at $V_{gs} = 0$ V, the Fermi level is located at the same position at negative and zero gate voltages. As shown in the inset of Fig. 2(b), at lower V_{gs}, the relatively weak built-in electric field formed between Te and MoS$_2$ enables photogenerated electron

transfer from Te to MoS$_2$ and generate smaller photocurrent. When V_{gs} increases, the Fermi level of MoS$_2$ is lifted up, and the enhanced vertical built-in field effectively facilitates the transfer of electrons from Te to MoS$_2$, resulting in the enhancement of photocurrent and responsivity. As V_{gs} increases to 80 V, R gradually approaches a saturated state, which can be attributed to the fast recombination between photogenerated holes and excess electrons in MoS$_2$, and the saturation of carrier mobility in MoS$_2$.[30] The relationship between responsivity and power density is presented in Fig. S6 in the supplementary material. As can be seen, the responsivity decreases as the power density increases. Under higher illumination intensity, the increase in the number of separated photo-generated carriers produces an electric field against the direction of the built-in electric field. The diminished built-in electric field then accelerates the carriers' recombination, which in turn leads to the decrement of responsivity. The specific detectivity (D^*) is another essential parameter for photodetectors. It can be calculated as

$$D^* = R\sqrt{\frac{S}{2qI_{dark}}} = \frac{I_{ph}}{\sqrt{I_{dark}}} \cdot \frac{1}{P\sqrt{2qS}},$$ (2)

in which R, S, q, and I_{dark} are the responsivity, the effective illumination area, the electron charge, and the dark current, respectively. As shown in Fig. 2(e), the maximal detectivity of 10^{12} Jones is obtained at $V_{gs} = 80$ V and $P = 0.299$ mW/cm^2. In addition, our hybrid device exhibits a calculated high photoconductive gain (G)[31] of over 10^3, which is defined as

$$G = \frac{Rhc}{q\lambda},$$ (3)

where h is the Planck constant, c is the light velocity, and λ is the light wavelength, as shown in Fig. 2(f), which is suggestive of the fact that more than 10^3 electrons can be achieved per photon at 1550 nm. Figure 3(a) presents the dynamic photocurrent response for a Te-MoS$_2$ hybrid phototransistor at a 1550 nm laser pulse with power densities of 6.55 and 24.95 mW/cm^2. An amplified photoresponse
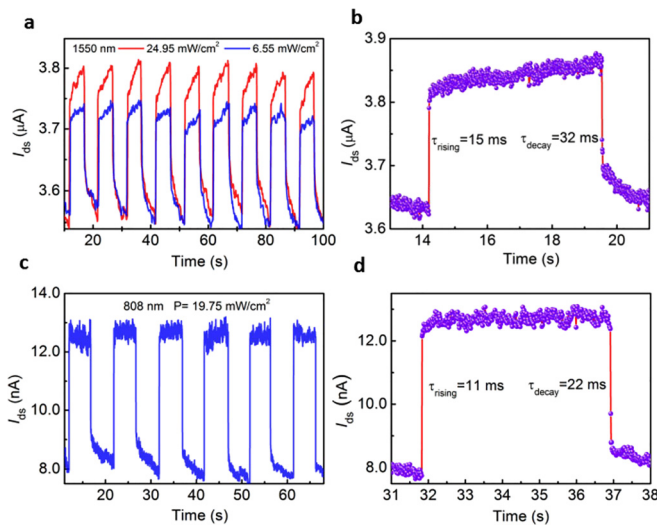
FIG. 3. (a) Dynamic photoresponse of Te nanowires-MoS$_2$ heterostructures was measured at 1550 nm with different power densities of 24.95 and 6.55 mW/cm^2 ($V_{ds} = 2$ V, $V_{gs} = 80$ V). (b) Temporal response shows $\tau_{rising} = 15$ ms and $\tau_{decay} = 32$ ms at 1550 nm. (c) Dynamic photoresponse at 808 nm with power density $P = 19.75$ mW/cm^2 ($V_{ds} = 2$ V, $V_{gs} = 20$ V). (d) Temporal response shows $\tau_{rising} = 11$ ms and $\tau_{decay} = 22$ ms at 808 nm.

cycle is given in Fig. 3(b); it exhibits a fast photoresponse speed ($\tau_{rising} = 15$ ms and $\tau_{decay} = 32$ ms), which is superior to the previously reported CQDs-based hybrid photodetectors.[7–10] Similarly, photoresponse of the Te-MoS$_2$ hybrid device to 808 nm was also measured. A stable photo-switching behavior can also be monitored at an incident power density of 19.75 mW/cm^2, as shown in Fig. 3(c). Figure 3(d) exhibits a faster response speed ($\tau_{rising} = 11$ ms and $\tau_{decay} = 22$ ms). As shown in Fig. S7(a) in the supplementary material, the rising and decay times can reach 4.59 ms and 9.16 ms, respectively, with the assistance of an oscilloscope. In addition, we also studied the effect of surface coverage of Te nanowires on photoresponse performance. The density of Te nanowires exhibited the tendency to increase with the reaction time (Fig. S8 in the supplementary material). As shown in Fig. S9(a) in the supplementary material, when the surface coverage is 30%, the rising and decay times of the Te/MoS$_2$ hybrid device are 23 and 39 ms, respectively. Faster response times ($\tau_{rising} = 23$ ms, $\tau_{decay} = 32$ ms and $\tau_{rising} = 15$ ms, $\tau_{decay} = 32$ ms) are obtained for the device with surface coverages of 50% and 60%, as observed in Figs. S9(b) and S9(c) in the supplementary material. The results indicate that the surface coverage dependence of response time is negligible. The responsivity of the device with different surface coverages was also calculated. As shown in Fig. S9(d) in the supplementary material, the responsivity shows obvious enhancement with the increase of the density of Te nanowires.

The comparison of individual Te and Te/MoS$_2$ heterostructure devices is given in Fig. S10 in the supplementary material. As shown in Figs. S10(a) and S10(b), the individual Te and Te/MoS$_2$ devices possess similar magnitudes of photocurrent and I_{ph} increases monotonically with power density P. For response time, as shown in Figs. S10(c) and S10(d), compared with Te/MoS$_2$ devices ($\tau_{rising} = 15$ ms and $\tau_{decay} = 32$ ms), individual Te shows a much slower response speed

($\tau_{rising} = 110$ ms, $\tau_{decay} = 170$ ms). This can be attributed to the fast recombination between photogenerated electrons and holes in Te. However, for Te/MoS$_2$ devices, the introduction of a vertical built-in field facilitates the rapid separation between photogenerated electrons and holes in Te. Besides, the strong vdWs coupling between the Te layer and the MoS$_2$ layer can effectively contribute to the interlayer charge transfer from Te to MoS$_2$, resulting in rapid response speed.[13] Due to the intrinsic small light absorption area of the Te nanowire, the responsivity of the individual Te device is slightly larger than the Te/MoS$_2$ hybrid device [Figs. S10(e) and S10(f)]. However, it is worth noting that the individual Te photodetector suffers from very high dark current [10^{-5}–10^{-6} A, Fig. S10(h)], leading to low detectivity [$\sim 10^{10}$ Jones, Fig. S10(f)] and a light switching ratio [~ 1.5, Fig. S10(h)]. In contrast, the Te/MoS$_2$ device shows higher detectivity [$\sim 10^{12}$ Jones, Fig. S10(e)] and a light switching ratio [~ 100, Fig. S10(g)] benefiting from MoS$_2$ as a conducting channel. Overall, the performance of the Te/MoS$_2$ device is superior to the individual Te device for infrared photodetection. Moreover, a comparison with previously reported infrared photodetectors is presented in Table I in the supplementary material. The overall performance of our device is found to be outstanding among the 2D infrared photodetectors. Compared with previous work, our work has made the following improvements: firstly, for the previous QDs-based hybrid photodetector, the traps at the interface can prolong the lifetime of the photocarriers and further severely slow the response speed. And, the interlayer charge transfer can be partially blocked due to the weak interfacial coupling.[32,33] Benefiting from the high-quality vdWs interface and effective interfacial coupling in our device, the response speed has been greatly improved. Then, for previous photodiodes, the potential barrier generated at the junction prevents the carrier recirculation and further restricts the gain,[6] in contrast to these photodiodes, MoS$_2$ operates in the conductor mode instead of the diode mode in our device, which promotes the responsivity.[34]

To further explore the origin of the outstanding photodetection ability in our hybrid device, the interfacial interaction modulated by the vdWs coupling was studied in the grown and the transferred Te-MoS$_2$ heterojunction. The means of deposition of the Te layer is crucial to the operation of the device. In the grown Te-MoS$_2$ heterojunction diode, significant anti-bipolar behavior[35–38] is observed when applying a reverse bias, as displayed in Fig. 4(a). As a result, with the moderate carrier density of both Te and MoS$_2$, the maximum value of drain current is obtained when $V_{gs} \approx 20$ V. And, the grown heterojunction also shows obvious rectification characteristic, and the highest rectification ratio of 10^3 is obtained under $V_{gs} = 80$ V, as shown in Fig. 4(b). But for the transferred Te-MoS$_2$ heterojunction, no obvious anti-bipolar behavior is observed [Fig. 4(c)], and these two semiconductors fail to produce an efficient rectifying heterojunction [Fig. 4(d)],[14] which also indicates that the rectification phenomenon comes mainly from the heterojunction region rather than the contact region. Based on the above discussion, the effective interfacial coupling in Te-MoS$_2$ heterostructures directly grown by CVD contributes to the rapid charge transfer at the interface, accompanied by the high infrared absorption in Te, leading to the outstanding photodetection ability of our device.

In conclusion, we demonstrated an infrared phototransistor based on a coupled Te-MoS$_2$ hybrid structure, in which Te nanowires are directly grown on MoS$_2$ via vdWs epitaxy. Benefiting from the
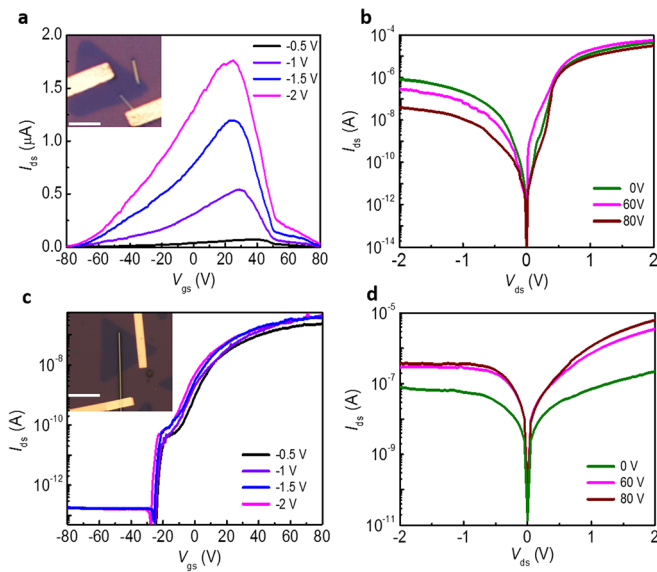
FIG. 4. (a) Transfer characteristic (I_{ds}–V_{gs}) measurements of the grown Te-MoS$_2$ heterojunction diode. The inset shows the OM image of the grown Te-MoS$_2$ heterojunction, the scale bar is 5 μm. (b) Output characteristic (I_{ds}–V_{ds}) measurements of the grown Te-MoS$_2$ heterojunction diode under different back-gated voltages V_{gs}. (c) Transfer characteristics (I_{ds}–V_{gs}) of the artificially transferred Te-MoS$_2$ heterojunction diode. The inset shows the OM image of the artificially transferred Te-MoS$_2$ heterojunction, the scale bar is 5 μm. (d) Output characteristic (I_{ds}–V_{ds}) measurements of the transferred Te-MoS$_2$ heterojunction diode.

strong vdWs coupling between the Te layer and the MoS$_2$ layer, the device exhibits not only ultrahigh photoresponsivity ($>10^3$ A/W) but also a rapid response time ($\tau_{rising} = 15$ ms) at the telecommunication wavelength of 1550 nm. Raman and PL studies indicate the effective interfacial coupling in the grown Te-MoS$_2$ heterojunction. And, the anti-bipolar and rectification behaviors observed in the strongly coupled grown Te-MoS$_2$ heterojunction further confirmed the existence of interfacial coupling. By comparison, the weakly coupled transferred Te-MoS$_2$ heterojunction exhibits negligible anti-bipolar behavior and slight rectification behavior. These results indicate that the coupled vdWs hybrid structures have significant potential for the next generation high-performance infrared detectors.

See supplementary material for more experimental details and device characterization.

REFERENCES

[1] L. Ye, H. Li, Z. Chen, and J. Xu, ACS Photonics **3**, 692 (2016).
[2] L. Ye, P. Wang, W. Luo, F. Gong, L. Liao, T. Liu, L. Tong, J. Zang, J. Xu, and W. Hu, Nano Energy **37**, 53 (2017).
[3] K. Zhang, T. Zhang, G. Cheng, T. Li, S. Wang, W. Wei, X. Zhou, W. Yu, Y. Sun, P. Wang, D. Zhang, C. Zeng, X. Wang, W. Hu, H. J. Fan, G. Shen, X. Chen, X. Duan, K. Chang, and N. Dai, ACS Nano **10**, 3852 (2016).
[4] X. Zhou, X. Hu, S. Zhou, H. Song, Q. Zhang, L. Pi, L. Li, H. Li, J. Lu, and T. Zhai, Adv. Mater. **30**, 1703286 (2018).
[5] M. Buscema, J. O. Island, D. J. Groenendijk, S. I. Blanter, G. A. Steele, H. S. van der Zant, and A. Castellanos-Gomez, Chem. Soc. Rev. **44**, 3691 (2015).
[6] D. Kufer and G. Konstantatos, ACS Photonics **3**, 2197 (2016).
[7] D. Zhang, L. Gan, Y. Cao, Q. Wang, L. Qi, and X. Guo, Adv. Mater. **24**, 2715 (2012).
[8] Z. Sun, Z. Liu, J. Li, G. A. Tai, S. P. Lau, and F. Yan, Adv. Mater. **24**, 5878 (2012).
[9] D. Kufer, I. Nikitskiy, T. Lasanta, G. Navickaite, F. H. Koppens, and G. Konstantatos, Adv. Mater. **27**, 176 (2015).
[10] C. Hu, D. Dong, X. Yang, K. Qiao, D. Yang, H. Deng, S. Yuan, J. Khan, Y. Lan, H. Song, and J. Tang, Adv. Funct. Mater. **27**, 1603605 (2017).
[11] W. Xu, W. Liu, J. F. Schmidt, W. Zhao, X. Lu, T. Raab, C. Diederichs, W. Gao, D. V. Seletskiy, and Q. Xiong, Nature **541**, 62 (2017).
[12] C. Jin, E. Y. Ma, O. Karni, E. C. Regan, F. Wang, and T. F. Heinz, Nat. Nanotechnol. **13**, 994 (2018).
[13] X. Hong, J. Kim, S.-F. Shi, Y. Zhang, C. Jin, Y. Sun, S. Tongay, J. Wu, Y. Zhang, and F. Wang, Nat. Nanotechnol. **9**, 682 (2014).
[14] V. Adinolfi and E. H. Sargent, Nature **542**, 324 (2017).
[15] Y. Du, G. Qiu, Y. Wang, M. Si, X. Xu, W. Wu, and P. D. Ye, Nano Lett. **17**, 3965 (2017).
[16] X. Huang, J. Guan, Z. Lin, B. Liu, S. Xing, W. Wang, and J. Guo, Nano Lett. **17**, 4619 (2017).
[17] Z. He, Y. Yang, J. W. Liu, and S. H. Yu, Chem. Soc. Rev. **46**, 2732 (2017).
[18] A. R. Jang, S. Hong, C. Hyun, S. I. Yoon, G. Kim, H. Y. Jeong, T. J. Shin, S. O. Park, K. Wong, S. K. Kwak, N. Park, K. Yu, E. Choi, A. Mishchenko, F. Withers, K. S. Novoselov, H. Lim, and H. S. Shin, Nano Lett. **16**, 3360 (2016).
[19] H. S. White, A. J. Rlcco, and M. S. Wrighton, J. Phys. Chem. **87**, 5140 (1983).
[20] M. K. Bahl, R. L. Watson, and K. J. Irgolic, J. Chem. Phys. **66**, 5526 (1977).
[21] K. Zhang, S. Hu, Y. Zhang, T. Zhang, X. Zhou, Y. Sun, T.-X. Li, H. J. Fan, G. Shen, X. Chen, and N. Dai, ACS Nano **9**, 2704 (2015).
[22] Q. S. Wang, M. Safdar, K. Xu, M. Mirza, Z. X. Wang, and J. He, ACS Nano **8**, 7497 (2014).
[23] A. S. Pine and G. Dresselhaus, Phys. Rev. B **4**, 356 (1971).
[24] D. H. Luong, H. S. Lee, G. P. Neupane, S. Roy, G. Ghimire, J. H. Lee, Q. A. Vu, and Y. H. Lee, Adv. Mater. **29**, 1701512 (2017).
[25] J. D. Lin, C. Han, F. Wang, R. Wang, D. Xiang, S. Qin, X.-A. Zhang, L. Wang, H. Zhang, A. T. S. Wee, and W. Chen, ACS Nano **8**, 5323 (2014).
[26] S. Mouri, Y. Miyauchi, and K. Matsuda, Nano Lett. **13**, 5944 (2013).
[27] Y. Liu, F. Wang, X. Wang, X. Wang, E. Flahaut, X. Liu, Y. Li, X. Wang, Y. Xu, Y. Shi, and R. Zhang, Nat. Commun. **6**, 8589 (2015).
[28] A. Castellanos-Gomez, E. Cappelluti, R. Roldan, N. Agrait, F. Guinea, and G. Rubio-Bollinger, Adv. Mater. **25**, 899 (2013).
[29] N. Huo and G. Konstantatos, Nat. Commun. **8**, 572 (2017).
[30] G. Fiori, B. N. Szafranek, G. Iannaccone, and D. Neumaier, Appl. Phys. Lett. **103**, 233509 (2013).
[31] F. H. Koppens, T. Mueller, P. Avouris, A. C. Ferrari, M. S. Vitiello, and M. Polini, Nat. Nanotechnol. **9**, 780 (2014).
[32] B. Y. Zhang, T. Liu, B. Meng, X. Li, G. Liang, X. Hu, and Q. J. Wang, Nat. Commun. **4**, 1811 (2013).
[33] J. Miao, W. Hu, N. Guo, Z. Lu, X. Liu, L. Liao, P. Chen, T. Jiang, S. Wu, J. C. Ho, L. Wang, X. Chen, and W. Lu, Small **11**, 936 (2015).
[34] Z. Chen, X. Li, J. Wang, L. Tao, M. Long, S. J. Liang, L. K. Ang, C. Shu, H. K. Tsang, and J. B. Xu, ACS Nano **11**, 430 (2017).
[35] M. H. Doan, Y. Jin, S. Adhikari, S. Lee, J. Zhao, S. C. Lim, and Y. H. Lee, ACS Nano **11**, 3832 (2017).
[36] A. Nourbakhsh, A. Zubair, M. S. Dresselhaus, and T. Palacios, Nano Lett. **16**, 1359 (2016).
[37] F. Wang, L. Yin, Z. X. Wang, K. Xu, F. M. Wang, T. A. Shifa, Y. Huang, C. Jiang, and J. He, Adv. Funct. Mater. **26**, 5499 (2016).
[38] Y. T. Lee, P. J. Jeon, J. H. Han, J. Ahn, H. S. Lee, J. Y. Lim, W. K. Choi, J. D. Song, M.-C. Park, S. Im, and D. K. Hwang, Adv. Funct. Mater. **27**, 1703822 (2017).